Simultaneous Observation of Columnar Defects and Magnetic Flux Lines in High-Temperature $Bi_2Sr_2CaCu_2O_8$ Superconductors

Hongjie Dai, Seokwon Yoon, Jie Liu, Ramesh C. Budhani, Charles M. Lieber*

Columnar defects generated by heavy-ion irradiation are promising structures for pinning magnetic flux lines and enhancing critical currents in superconductors with high transition temperatures. An approach that combines chemical etching and magnetic decoration was used to highlight simultaneously the distributions of columnar defects and magnetic flux lines in $Bi_2Sr_2CaCu_2O_8$ superconductors. Analyses of images of the columnar defects and flux-line positions provide insight into flux-line pinning by elucidating (i) the occupancy of columnar defects by flux lines, (ii) the nature of topological defects in the flux-line lattice, and (iii) the translational and orientational order in this lattice.

Large critical current densities (J_c) in the presence of magnetic fields are essential to many proposed applications of the high–transition temperature (T_c) copper oxide superconductors. In general, J_c is limited by the motion of magnetic flux lines because this motion causes finite electrical resistance (*1*, *2*). To obtain large J_c values requires the pinning of flux lines to the crystal lattice. A promising approach to this challenging and technologically important problem involves the creation of correlated defects, such as columnar structures, in the crystal lattice (*3*–*6*). Columnar defects consisting of linear damage tracts ~100 Å in diameter and tens of micrometers in length can be produced by heavy-ion bombardment at energies on the order of several hundred megaelectron volts (*7*). Qualitatively, the interaction of a flux line with such a linear defect should result in a pinning energy that is much larger than what would be obtainable by use of a random array of point defects. The effectiveness of columnar defects at enhancing J_c has been demonstrated experimentally in $YBa_2Cu_3O_7$ (*4*), $Tl_2Ba_2CaCu_2O_8$ (*5*), and $Bi_2Sr_2CaCu_2O_8$ (*6*) high-T_c superconductors (*8*).

To understand the origin of these results requires an understanding of the structure and interactions of the flux-line lattice (FLL) with columnar defects. Nelson and Vinokur have developed a theoretical model for flux-line pinning by correlated defects that predicts equilibrium FLL structures and dynamic properties as a function of temperature and magnetic field (*9*). Transport studies (*10*) are consistent with some of these predictions. However, experimental knowledge of the microscopic distribution of defects and the interaction of these defects with flux lines is virtually nonexistent (*11*). Such detailed information is critical for testing theoretical models and for guiding experimental efforts to improve further flux-line pinning and J_c values in the copper oxide materials.

To this end we report experimental studies that elucidate the distributions of both columnar defects and flux lines as a function of the defect density in $Bi_2Sr_2CaCu_2O_8$ (BSCCO) superconductors. The distributions of columnar defects at the surfaces of BSCCO single crystals were imaged by atomic force microscopy (AFM) after these defects had been preferentially etched. These data were fitted to a Poisson distribution, although potentially important deviations were found for small wave vectors. The flux-line positions, which were highlighted by decoration with magnetic particles, were imaged simultaneously with columnar defects by scanning electron microscopy (SEM) and AFM. Quantitative image analysis was used to characterize the occupancy of columnar defects by flux lines and the structural properties of the FLL.

Reported procedures (*12*) were used to grow and anneal single crystals of BSCCO. We created columnar pins by irradiating cleaved BSCCO crystals along the *c* axis with 276-MeV Ag ions at Brookhaven National Laboratory (*7*). The columnar defect densities calculated from the ion-beam fluences and irradiation times were 1.5×10^7 and 5×10^8 defects per square centimeter, respectively. The corresponding matching magnetic fields (one flux line per defect) are B_Φ = 3.6 and 118 G, respectively. We etched irradiated crystals using a Na_2EDTA solution (*13*) to preferentially remove material at the columnar defect sites, and the crystals were imaged by AFM. We highlighted the positions of flux lines in the irradiated BSCCO samples by evaporating magnetic iron clusters onto the crystal surfaces at 4.2 K (applied magnetic field, H, is parallel to the *c* axis) to form Bitter patterns (*1*, *12*). We imaged the FLL patterns at room temperature using AFM or SEM.

Images of etched samples containing columnar defects exhibit pits on the crystal surfaces (Fig. 1, A and B), whereas the surfaces of unirradiated samples remain smooth after etching. The columnar defects are preferentially etched because they consist of damaged amorphous material (*7*). The pits typically have an inverted pyramid shape (*14*), and their size depends reproducibly on the etching time. For example, samples etched for 3 min and 1 min exhibit pits with bases per depth of 1.6 μm per 0.25 μm and 0.45 μm per 0.035 μm, respectively (Fig. 1). Smaller etch pits can be obtained if shorter etching times or lower solution concentrations are used. We analyzed the columnar defect densities after locating the

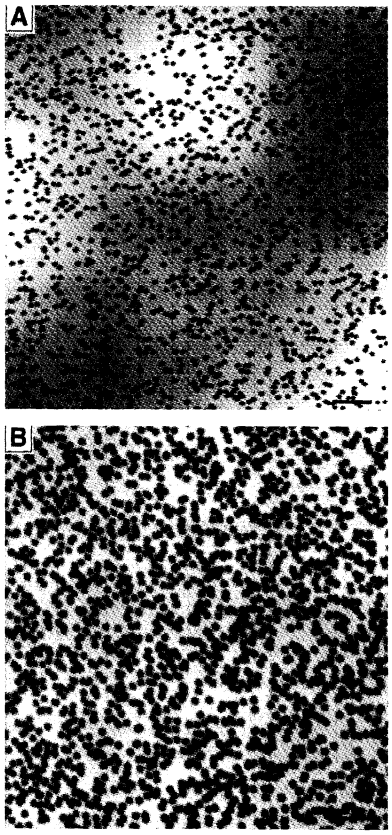

Fig. 1. AFM images recorded on etched surfaces of BSCCO single crystals that were irradiated with 276-MeV Ag^{21+} ions to produce columnar defect densities of (**A**) 1.5×10^7 and (**B**) 5×10^8 defects per square centimeter. The columnar defects, which are preferentially etched to form pits on the crystal surfaces, appear as small red-orange spots in these pseudo gray-scale images. We etched the crystals using oxygen-free 1.7×10^{-3} M Na_2EDTA solutions for 3 min in (A) and 1 min in (B). After etching, the crystal surfaces were washed with deionized water and dried in nitrogen gas. Images were recorded in air with a Nanoscope III atomic force microscope using Si_3N_4 cantilevers. The black scale bars in (A) and (B) correspond to 10 μm and 2 μm, respectively.

H. Dai, S. Yoon, J. Liu, C. M. Lieber, Division of Applied Sciences and Department of Chemistry, Harvard University, Cambridge, MA 02138, USA.
R. C. Budhani, Department of Physics, Indian Institute of Technology, Kanpur 208016, India.
*To whom correspondence should be addressed.

center of mass of each defect in the digital images (*15*). The densities of defects calculated for two types of samples were 1.6×10^7 and 4.6×10^8 defects per square centimeter. These values agree well with those estimated from the irradiation doses: 1.5×10^7 and 5×10^8 defects per square centimeter, respectively. These results demonstrate that our chemical etching procedure highlights essentially all of the columnar defects in the samples.

We have also investigated the distribution of columnar defects in the samples. First, a density distribution function, $P(N)$, defined as the probability of finding N defects in a unit area within an image, was determined (Fig. 2A). Under the assumption that the defects are distributed randomly, these data were fitted to a Poisson distribution

$$P(N) = \langle N \rangle^N \cdot e^{-\langle N \rangle}/N!$$

(where $\langle N \rangle$ is the mean number of defects in a unit area). Fits using the Poisson distribution agree reasonably well with the experimental data, although there are deviations. To examine further defect distribution, we have calculated the structure function

$$S(\mathbf{k}) = \langle \rho(\mathbf{k}) \cdot \rho(-\mathbf{k}) \rangle / N_D$$

where N_D is the total number of defects in an image and

$$\rho(\mathbf{k}) = \sum_{i=1}^{N_D} \exp(i\mathbf{k} \cdot r_i)$$

is the Fourier transform of the defect positions (*16*). A plot of $S(k)$ averaged over angle is shown in Fig. 2B. It is expected that $S(k) \approx 1$ for a Poisson distribution except at $k \approx 0$ where it will rise as a delta function (*16*). Our experimental data show, however, that $S(k)$ drops below unity for $k < 2 \cdot 2\pi/d$, where d is the average defect spacing. This result indicates that there is correlation in the distribution of columnar defects that could arise from long-range coulomb interactions between ions in the beam

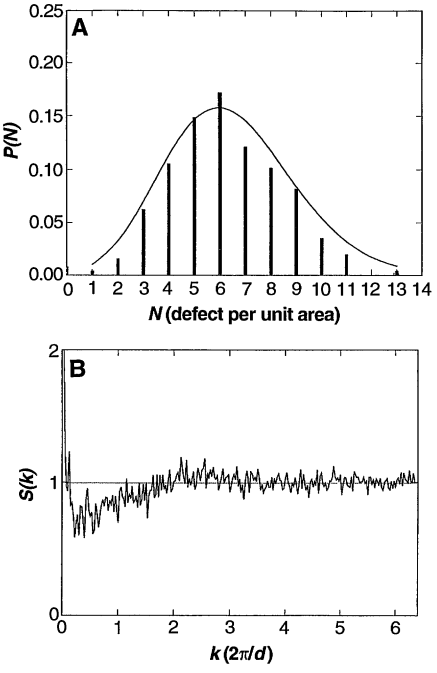

Fig. 2. (**A**) Plot of the probability, $P(N)$, of finding N defects in a unit area. The data were determined from Fig. 1A using a unit area of ~39 μm^2; $P(N)$ was found to be similar for areas between 9.8 and 156 μm^2. The smooth black curve corresponds to a fit using a Poisson distribution, where $\langle N \rangle$/unit area (=1.6×10^7 defects per square centimeter) agrees well with the average columnar defect density. (**B**) Plot of the structure factor calculated from the data in Fig. 1A versus $k = 2\pi/d$, where d is the average defect spacing.

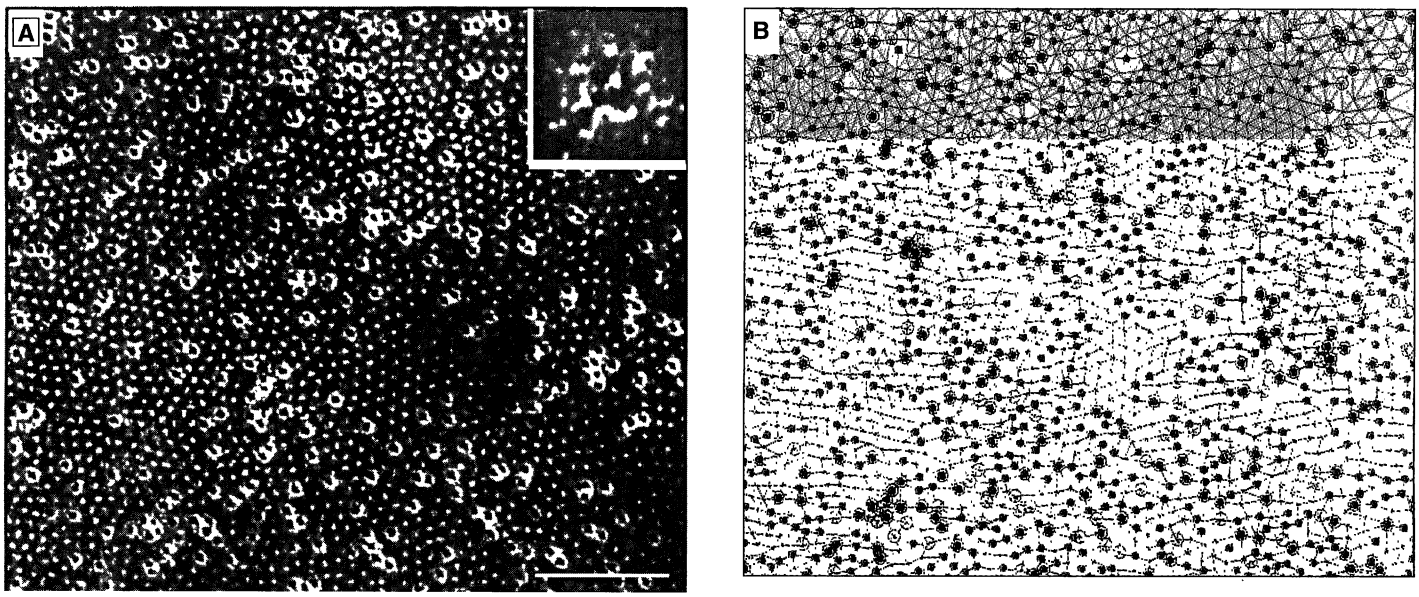

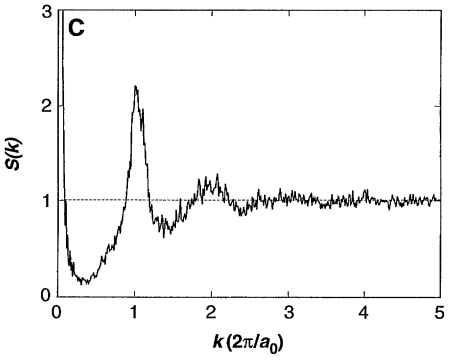

Fig. 3. (**A**) SEM image of an etched BSCCO sample containing 1.6×10^7 columnar defects per square centimeter that was decorated with magnetic iron clusters in an applied field of 16.5 G. Flux lines not lying directly on columnar defects appear as small light spots, whereas flux lines emanating from the columnar defects appear as light rings surrounding dark spots that correspond to the etch pits. The inset shows a high-resolution image of a flux line emanating from an etched columnar defect site. This image, which was focused at the center of the etch pit, shows that there is a magnetic cluster at the center (bottom) of the pit. The white scale bar in (A) corresponds to 10 μm. (**B**) Delaunay triangulation of the image in (A). In the triangulation each flux line corresponds to the vertex formed by bonds drawn from the flux line to its nearest neighbors. In this image, columnar defects are denoted by open red circles, flux lines without sixfold coordination are marked with blue circles, and isolated disclinations are highlighted by yellow shading. (**C**) Plot of the structure factor calculated from the data in Fig. 3A versus $k = 2\pi/a_0$, where a_0 is the average flux-line spacing.

used to irradiate the samples (*17*). Importantly, manipulation of the distribution of columnar defects (for example, by controlling the ion beam to make a more regularly spaced array of defects) could be used to enhance pinning and J_c.

To study flux-line pinning by columnar defects, we have analyzed the Bitter patterns formed on these samples. A typical example of the Bitter patterns recorded on a sample etched for 80 s is shown in Fig. 3A. The average FLL constant in Fig. 3A is a_0 = 1.1 μm, and the average columnar defect spacing is d = 2.5 μm; this regime is called "overfilled" to reflect the excess of flux lines relative to defects. The key feature of images such as Fig. 3A is that they resolve simultaneously the positions of both flux lines and columnar defects. The positions of flux lines not lying directly on columnar defects appear as small light spots ~0.3 μm in diameter. The flux lines emanating from the etch pits that mark the columnar defects appear as light rings surrounding the dark spots that correspond to the pits. The ring structure marking flux lines at the surface of the etch pits is expected because the magnetic field from a pinned flux line emanating from the bottom of a pit will spread and have a large gradient (which attracts iron particles strongly) at the surface. High-resolution images (inset in Fig. 3A) also show that clusters of magnetic particles sit near the centers of the etch pits, thus confirming that the ring structures correspond to the flux-line positions (*18*). Interestingly, qualitative analysis of this image demonstrates that two columnar defect sites may both be occupied even when the defect spacing is less than the average flux-line spacing.

To learn more about the microscopic structure of the pinned FLL, we have characterized topological defects in the lattice using Delaunay triangulations of the Bitter patterns (*15*). For the triangulation shown in Fig. 3B, topological defects (that is, flux lines without sixfold coordination) are highlighted by solid blue circles and columnar defects are indicated by open red circles. This analysis shows that (i) each columnar defect is occupied by a flux line, (ii) adjacent columnar defects can expand or compress the local FLL constant, and (iii) there are numerous topological defects, including dislocations and high-energy disclinations, in the FLL (*19*). In addition, small crystalline FLL domains are present in regions free of columnar defects for this overfilled regime. Significantly, the topological defects are expected to destroy long-range order in the FLL.

To assess quantitatively the translational order in the pinned FLL, we have calculated $S(k)$ from the flux-line positions identified in Fig. 3B. The powder-averaged $S(k)$ plotted in Fig. 3C exhibits a broad first-order peak at $k = 2\pi/a_0$ from which we estimate a translational correlation length of $\xi_T = 2.5a_0$. This result illustrates further the strong pinning exerted by the columnar defects because it is the average columnar defect spacing, $2.5a_0$, that appears to set ξ_T. In addition, we have evaluated the orientational order of the FLL (*20*). Earlier studies of BSCCO superconductors containing point impurities have suggested that the FLL structure is a hexatic glass that has short-range translational order but long-range orientational order. The orientational correlation length in these samples containing columnar defects, $\xi_6 = 2.33a_0$, is very short and also similar to the average defect spacing; that is, the FLL does not have long-range orientational order (*21*). Hence, in the regime where $B > B_\phi$, the FLL has a glassy or amorphous structure.

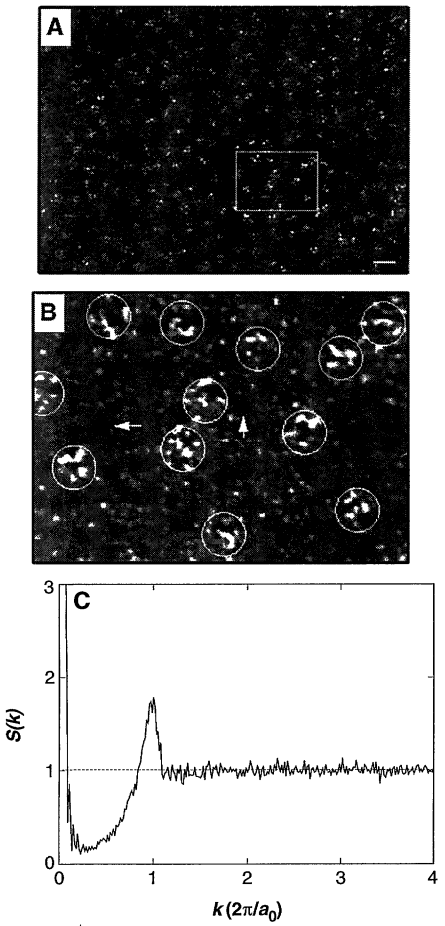

Fig. 4. (**A**) SEM image of an etched BSCCO sample containing 4.6 × 10^8 columnar defects per square centimeter that was decorated with magnetic iron clusters in an applied field of 33 G. The flux-line positions appear as light spots in the image. The average flux-line spacing in this image is 0.8 μm, and the average defect spacing is 0.47 μm; thus, the areal density of columnar defects exceeds that of flux lines by a factor of 2.9. The white scale bar corresponds to 1 μm. (**B**) High-resolution image corresponding to the rectangular box outlined in (A). The etched columnar defect sites appear as small dark circles ~0.2 μm in diameter; arrows mark two of the unoccupied sites. Open white circles highlight the flux-line positions. (**C**) Plot of the structure factor calculated from an image, which was obtained from the same sample as (A), containing ≈1000 flux lines.

Lastly, to demonstrate the generality of our approach, we have carried out preliminary studies in the regime where the density of columnar defects is greater than that of flux lines ($B < B_\phi$). Representative images of a Bitter pattern obtained on a crystal etched for 50 s are shown in Fig. 4, A and B; the sample contains 4.6 × 10^8 defects per square centimeter. The positions of flux lines appear as small light spots in large-area images (Fig. 4A), although high-resolution images (Fig. 4B) show that each of these spots consists of a ring-like structure around an etch pit. The positions of the etched columnar defects appear as small dark circles ~0.2 μm in diameter in these images. Qualitatively, the FLL appears completely disordered, as might be expected for strong pinning by an essentially random distribution of defects. A similar finding was reported recently (*22*), although the positions of columnar defects were not identified.

It is also interesting to consider whether interactions other than pinning are important because it is clear from our data that flux lines occupy only specific defect sites. To address this point, we have calculated $S(k)$ (Fig. 4C). We find that $S(k)$ shows a pronounced first-order peak at $k = 2\pi/a_0$, which demonstrates that the FLL has remnant correlation despite the random distribution of pinning sites. Importantly, this observation shows that the flux lines must preferentially occupy only certain columnar defect sites and indicates that the long-range repulsive interaction between flux lines still plays an important role in determining the FLL structure in this underfilled regime (*23*).

In summary, our experimental approach allows for the simultaneous characterization of the distributions of columnar defects and flux lines in high-T_c copper oxide superconductors. Significantly, with this approach it has been possible to evaluate the structure, pinning, and correlations within the FLL in microscopic detail. The structural results available from these studies will make possible the direct calculation of transport properties from the distributions of occupied and unoccupied columnar defect sites (*24*). More generally, our methodology can be used to map out systematically the phase diagram for the FLL in copper oxide superconductors containing columnar pins.

Such results will be critical for assessing experimentally the nature of pinning by correlated defects, for testing (and guiding) theories that are being developed to understand these systems, and for devising methods for enhancing further critical currents in the high-T_c materials.

REFERENCES AND NOTES

1. D. J. Bishop, P. L. Gammel, D. A. Huse, C. A. Murray, *Science* **255**, 165 (1992).
2. D. A. Huse, M. P. A. Fisher, D. S. Fisher, *Nature* **358**, 553 (1992).
3. G. Taubes, *Science* **261**, 1521 (1993).
4. L. Civale *et al.*, *Phys. Rev. Lett.* **67**, 648 (1991).
5. R. C. Budhani, M. Suenaga, S. H. Liou, *ibid.* **69**, 3816 (1992).
6. W. Gerhauser *et al.*, *ibid.* **68**, 879 (1992).
7. Y. Zhu, Z. X. Cai, R. C. Budhani, M. Suenaga, D. O. Welch, *Phys. Rev. B* **48**, 6436 (1993).
8. Columnar defects also shift the apparent irreversibility line, which defines the boundary in the magnetic field–temperature plane between reversible and irreversible flux motion, upward in these materials.
9. D. R. Nelson and V. M. Vinokur, *Phys. Rev. Lett.* **68**, 2398 (1992); *Phys. Rev. B* **48**, 13060 (1993).
10. W. Jiang *et al.*, *Phys. Rev. Lett.* **72**, 550 (1994); R. C. Budhani, W. L. Holstein, M. Suenaga, *ibid.*, p. 566.
11. S. Behler *et al.*, *ibid.*, p. 1750.
12. H. Dai, J. Liu, C. M. Lieber, *ibid.*, p. 748.
13. D. S. Ginley *et al.*, *J. Mater. Res.* **9**, 1126 (1994).
14. AFM images acquired with the sample rotated at different angles while keeping the scan direction the same with respect to the tip demonstrated that the shape of the etch pits is intrinsic and does not reflect a convolution of the tip geometry. SEM and optical microscopy studies also support the inverted pyramid geometry assigned to the pits.
15. H. Dai and C. M. Lieber, *Annu. Rev. Phys. Chem.* **44**, 237 (1993).
16. J. P. Hansen and I. R. McDonald, *Theory of Simple Liquids* (Academic Press, New York, 1976).
17. D. R. Nelson, *Physica A* **177**, 220 (1991).
18. Images recorded in the regime where the areal defect density is greater than the flux-line density show that only some of the etch pits are decorated by magnetic particles (for example, Fig. 4A). These results show that it is not simply the presence of etch pits that attracts the particles; a flux line must also exist on the columnar defect site.
19. Because the same density of FLL topological defects is observed on unetched samples, we believe that the etch pits do not affect the overall FLL structure.
20. The orientational correlation function is defined as
$$G_6(\mathbf{r}) = \langle \psi_6^*(0)\psi_6(\mathbf{r})\rangle$$
where the orientational order parameter
$$\psi_6(\mathbf{r}) = \sum_{i=1}^{n} \exp[i6\theta_i(\mathbf{r})]/n$$
is summed over all n nearest neighbors of a vortex at $\mathbf{r}$ (*15*). For the samples containing columnar defects, the orientational correlation function can be fitted to an exponential,
$$G_6(r) \propto \exp(-r/\xi_6)$$
where the correlation length, ξ_6, equals the average defect spacing.
21. The same values of ξ_T and ξ_6 were determined from analyses of Bitter patterns formed on unetched samples. These results quantitatively confirm that the etch pits do not affect the overall FLL structure.
22. M. Leghissa, L. A. Gurevich, M. Kraus, G. Saemann-Ischenko, L. Y. Vinnikov, *Phys. Rev. B* **48**, 1341 (1993).
23. The long-range interaction depends logarithmically on separation, $\ln(r/\lambda)$, and should become important when $a_0 \leq \lambda$, the magnetic penetration depth. This criterion seemingly is not met in our decoration experiments carried out at 4.2 K where $\lambda \approx 0.2\ \mu m < a_0$. However, if the FLL structure is frozen at a higher temperature, the results are understandable because λ diverges with temperature as
$$\lambda(T) \cong \lambda(0)\cdot[1-(T/T_c)^4]^{-1/2}$$
in the two-fluid model. Using this expression to estimate the temperature where $a_0 \approx \lambda$ yields $T = 0.98\ T_c$; this value is close to the apparent irreversibility temperature (at the corresponding field) for these samples.
24. U. Tauber, H. Dai, D. R. Nelson, C. M. Lieber, unpublished material.

25. We thank D. R. Nelson and U. Tauber for helpful discussions. C.M.L. acknowledges support by the National Science Foundation (grant DMR 9306684) and the Harvard Materials Research Laboratory.

20 May 1994; accepted 18 July 1994

Lattice Location of Trace Elements Within Minerals and at Their Surfaces with X-ray Standing Waves

Yonglin Qian, Neil C. Sturchio, Ronald P. Chiarello, Paul F. Lyman, Tien-Lin Lee, Michael J. Bedzyk*

The x-ray standing waves generated by dynamical Bragg diffraction were used to directly measure lattice locations of trace elements within and at the surface of a mineral single crystal. These high-precision measurements were made on natural Iceland spar calcite cleaved along the (10$\bar{1}$4) plane and reacted with a dilute aqueous lead solution. Within the bulk crystal, naturally occurring trace manganese was found within (10$\bar{1}$4) planes, consistent with its substitution for calcium. At the crystal surface, sorbed lead was found to be highly ordered and mostly within (10$\bar{1}$4) planes. This demonstrates a powerful application of synchrotron radiation in the earth and environmental sciences.

Knowledge of the crystallographic locations of minor and trace elements within minerals and at their surfaces is important for a wide range of applications in the earth and environmental sciences. This knowledge facilitates a more rigorous understanding of dynamic natural processes (for example, the genesis of rocks and minerals, the transport of contaminants in ground waters, biomineralization, and the history of Earth's climate). The classical approach to determining sites of elements in minerals combines x-ray diffraction structure refinements with bulk chemical analyses and crystal-chemical reasoning. As a complement to this approach, a range of spectroscopic methods allowing improved solid-state characterization has gained widespread use during recent decades (*1*).

Atomic-scale processes at mineral surfaces have been receiving increased attention because of their importance in environmental geochemistry. This has been stimulated by the advent of new techniques and facilities, such as atomic force microscopy and high-brilliance synchrotron radiation sources, which allow unprecedented studies of atomic-scale processes at mineral surfaces (*2–5*). This report demonstrates an additional technique involving the use of x-ray standing waves as an element-specific structural probe to directly provide precise (~0.04 Å) data on the crystallographic site locations of trace elements in minerals and at their surfaces.

On the basis of von Laue and Ewald's dynamical theory for x-ray diffraction (*6*), Batterman (*7*) demonstrated that an x-ray standing wave (XSW) is generated inside a perfect single crystal during Bragg diffraction. Later, Cowan, Golovchenko, and Robbins (*8*) showed that the XSW not only exists inside the crystal but also extends above the surface (Fig. 1). The length scale of the standing wave probe is characterized by its period, which is equal to the d spacing of the diffraction planes. Rocking the crystal in angle θ (or scanning the incident photon energy) through the Darwin curve of a strong Bragg reflection causes the antinodes of the standing wave to shift inward by one-half of a period. By monitoring the modulation of the fluorescence yield from a specific atomic species while phase-shifting the XSW, one can determine the atomic position (or distribution) relative to the bulk diffraction plane. Thus, the XSW method directly solves the "phase problem" inherent to conventional diffraction methods and has proven to be a highly precise probe for measurement of the positions of impurity atoms at the surface and within artificially grown perfect single crystals (*7–11*).

For this experiment, we used natural calcite (Fig. 1). The rhombohedral calcite

Y. Qian and M. J. Bedzyk, Materials Science Division, Argonne National Laboratory, Argonne, IL 60439, and Department of Materials Science and Engineering and Materials Research Center, Northwestern University, Evanston, IL 60208, USA.
N. C. Sturchio and R. P. Chiarello, Geoscience/CMT-205, Argonne National Laboratory, Argonne, IL 60439, USA.
P. F. Lyman and T.-L. Lee, Department of Materials Science and Engineering and Materials Research Center, Northwestern University, Evanston, IL 60208, USA.
*To whom correspondence should be addressed.